Supporting Information

Formation and Fine-tuning of Metal-Organic Frameworks with Carboxylic Pincers for the Recognition of a C_2H_2 Tetramer and Highly Selective Separation of C_2H_2/C_2H_4

Yuefeng Duan[a,c], Yuhang Huang[a,c], Chongqing Wang[a], Qian Wang[b], Kai Ge[a], Zhiyong Lu[b], Huijie Wang[a], Jingui Duan[a,*], Junfeng Bai[b,*], Wanqin Jin[a]

[a] State Key Laboratory of Materials-Oriented Chemical Engineering, College of Chemical Engineering, Nanjing Tech University, Nanjing 211816, China.

[b] School of Chemistry and Molecular Engineering, Nanjing Tech University, Nanjing 211816, China.

[c] They contribute equally to this work.

Email: duanjingui@njtech.edu.cn; bjunfeng@njtech.edu.cn

General procedures and materials

All the solvents and materials were purchased from chemical vendors and without further depuration before used. The instrument used for the 1H-NMR test was a Bruker Advance III 600 MHz nuclear magnetic resonance spectrometer. Powder X-Ray Diffraction (PXRD) pattern was tested with Rigaku SmartLab3 (test conditions: 40 kV, 40 mA, CuKα, λ = 1.5418 Å, scanning range 5-50°). Infrared (FT-IR) spectra were tested on the VECTOR 22 spectrometer using KBr tableting method in the range of 4000-400 cm^{-1}. Thermogravimetric analysis (TGA) measurements were performed on a STA 209 F1 instrument under astatic N_2 atmosphere with a heating rate of 10 °C/min at the range of 30−600 °C. Raman spectra of gas loaded samples were collected on a Horiba Jobin-Yvon HR800 Raman Spectrometer at 298 K, 1 bar.

Ligand synthesis

3,5-di (1H-imidazol-1-yl) benzoic acid was prepared according to our previous work.[1]

Crystal analysis

Single-crystal X-ray diffraction data was collected by a Bruker Smart Apex CCD diffractometer at 298 K using graphite monochromator Mo Kα radiation (λ = 0.71073 Å). Data reduction was made with the Bruker Saint program. The structure was solved by direct methods and refined with full- matrix least-squares technique using the SHELXTL package.[2] Non-hydrogen atoms were refined with anisotropic displacement parameters during the final cycles. Organic hydrogen atoms were placed in calculated positions with isotropic displacement parameters set to 1.2 × Ueq of the attached atom. We have employed PLATON/SQUEEZE[3, 4] to calculate the diffraction contribution of the solvent molecules and, thereby, to produce a set of solvent-free diffraction intensities; structures were then refined again using the data generated. Crystal data are summarized in Table S1.

Table S1. Crystal data and structure refinement parameters for **NTU-71** to **NTU-73**.

	NTU-71	**NTU-72**	**NTU-73**	**NTU-72⊃C_2H_2**	**NTU-72⊃C_2H_4**	**NTU-72⊃H_2O**
Empirical formula	$C_{26}H_{20}Cu_2F_6N_8O_4Si$	$C_{26}H_{20}Cu_2F_6N_8O_4Ti$	$C_{26}H_{20}Cu_2F_6N_8O_4Zr$	$C_{26}H_{20}CuF_6N_8O_4Ti$, C_2H_2	$C_{26}H_{20}CuF_6N_8O_4$ Ti, 0.5C_2H_4	$C_{26}H_{20}CuF_6N_8O_4$ Ti, 4H_2O
Formula weight	714.14	733.92	777.27	758.95	747.95	805.98
Space group	$I4_122$	$I4_122$	$I4_122$	$I4_122$	$I4_122$	$I4_122$
a / Å	16.228(4)	16.748 (10)	16.848 (5)	16.619(3)	16.567(2)	16.542(4)
b / Å	16.228(4)	16.748 (10)	16.848 (5)	16.619(3)	16.567(2)	16.542(4)
c / Å	32.536(18)	32.240 (5)	31.093 (17)	31.843(10)	31.995(9)	31.799(14)
Crystal System	tetragonal	tetragonal	tetragonal	tetragonal	tetragonal	tetragonal
V/Å^3	8568(6)	9043(18)	8826(7)	8795(4)	8782(3)	8701.6(6)
Z	8	8	8	8	8	8
Density/g cm^{-3}	1.107	1.078	1.170	1.146	1.131	1.230
	-19≤ h ≤19	-19≤ h ≤19	-21≤ h ≤21	-21≤ h ≤21	-19≤ h ≤19	-13≤ h ≤19
Index ranges	-19≤ h ≤18	-19≤ h ≤18	-21≤ k ≤20	-21≤ k ≤20	-19≤ h ≤18	-19≤ h ≤19
	-38≤ h ≤38	-38≤ h ≤38	-40≤ l ≤40	-40≤ l ≤39	-38≤ h ≤38	-37≤ h ≤37
R_1	0.0804	0.0604	0.0583	0.0726	0.0706	0.0773
wR_2 [I>2σ(I)]	0.2001	0.1211	0.1283	0.2299	0.1887	0.2419
F(000)	2888	2952	3096	3056	3016	3272
GOOF	1.04	1.04	1.04	1.112	1.07	1.08

$R = \Sigma||F_o|-|F_c||/\Sigma|F_o|$, $wR = \{\Sigma[w(|F_o|^2 - |F_c|^2)^2]/\Sigma[w(|F_o|^4)]\}^{1/2}$ and $w = 1/[\sigma^2(F_o^2) + (0.1452P)^2]$ where $P = (F_o^2+2F_c^2)/3$

Sample activation

Prior to adsorption measurement, the samples were prepared by immersing the as-synthesized samples in dry Acetone for three days to remove non-volatile solvents, and the extract was decanted every 8 h and replaced with fresh Acetone. The completely activated sample was obtained by heating the solvent-exchanged sample at 25 °C under a dynamic high vacuum for 24 h.

Single gas adsorption

In the gas adsorption measurement, ultra-high-purity grade of CO_2, C_2H_2, and C_2H_4 gases were used throughout the adsorption experiments. Gas adsorption isotherms were obtained using a Belsorp-mini volumetric adsorption instrument from BEL Japan Inc, using the volumetric technique.

Estimation of the isosteric heats of gas adsorption

A virial-type expression comprising the temperature-independent parameters a_i and b_i was employed to calculate the enthalpies of adsorption for C_2H_2 and C_2H_4 (at 273 and 298 K) on **NTU-71**, **NTU-72** and **NTU-73**. In each case, the data were fitted using the equation (1):

$$\ln P = \ln N + 1/T \sum_{i=0}^{m} a_i N^i + \sum_{i=0}^{n} b_i N^i \qquad (1)$$

Here, *P* is the pressure expressed in Torr, *N* is the amount adsorbed in mmol g^{-1}, *T* is the temperature in K, a_i and b_i are virial coefficients, and *m*, *n* represent the number of coefficients required to adequately describe the isotherms (*m* and *n* were gradually increased until the contribution of extra added *a* and *b* coefficients were deemed to be statistically insignificant towards the overall fit, and the average value of the squared deviations from the experimental values was minimized).

$$Q_{st} = -R \sum_{i=0}^{m} a_i N^i \qquad (2)$$

Here, Q_{st} is the coverage-dependent isosteric heat of adsorption and *R* is the universal gas constant (2).

Selectivity Prediction for Binary Mixture Adsorption

Ideal adsorbed solution theory (IAST) was used to predict binary mixture adsorption from the experimental pure-gas isotherms. To perform the integrations required by IAST, the single-component isotherms should be fitted by a proper model. There is no restriction on the choice of the model to fit the adsorption isotherm, however, data over the pressure range under study should be fitted very precisely. Several isotherm models were tested to

fit the experimental pure isotherms for C_2H_2 and C_2H_4 of **1**, and the dual-site Langmuir-Freundlich equation (3) were found to the best fit to the experimental data:

$$q = q_{m1} \cdot \frac{b_1 \cdot P^{1/n_1}}{1 + b_1 \cdot P^{1/n_1}} + q_{m2} \cdot \frac{b_2 \cdot P^{1/n_2}}{1 + b_2 \cdot P^{1/n_2}} \quad (3)$$

Here, P is the pressure of the bulk gas at equilibrium with the adsorbed phase (kPa), q is the adsorbed amount per mass of adsorbent (mol kg^{-1}), q_{m1} and q_{m2} are the saturation capacities of sites 1 and 2 (mol kg^{-1}), b_1 and b_2 are the affinity coefficients of the sites (1/kPa), and n_1 and n_2 are measures of the deviations from an ideal homogeneous surface. The R_2 values for all of the fitted isotherms were over 0.99997. Hence, the fitted isotherm parameters were applied to perform the necessary integrations in IAST.

Breakthrough measurements

The breakthrough experiments were performed on the Beifang Gaorui CT-4 system. Mass flow controllers regulate the flow rates of all gases. Effluent gas stream from the column is monitored by gas chromatography (GC) detector. The initial activated **NTU-72** crystals were packed into a stainless-steel column (φ = 3 mm, L= 20 cm). The sample was activated at 40°C under a dynamic vacuum for 2 days. After the temperature cooling down, helium flow was introduced into the system for pressure compensation and then the feed gas was changed to C_2H_2/C_2H_4 mixtures.

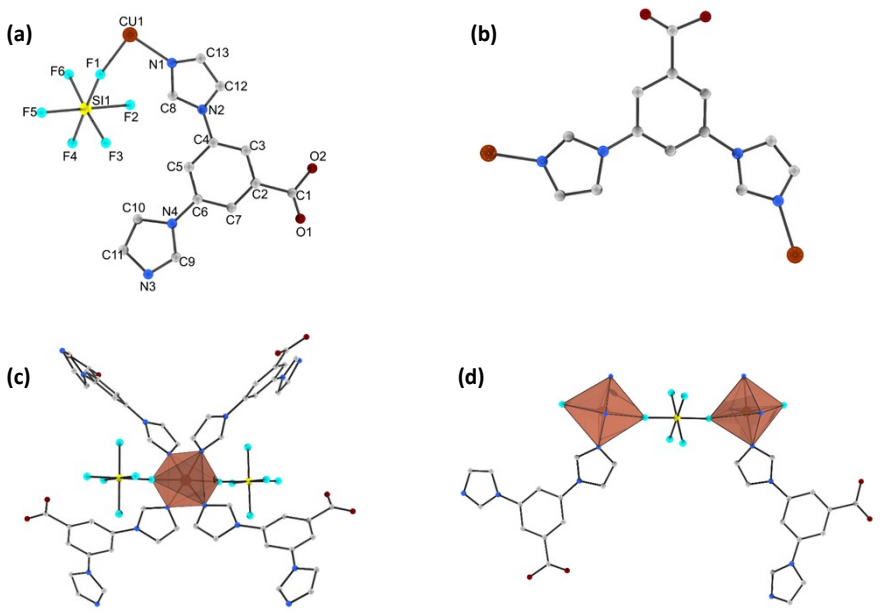

Figure S1. Structure of **NTU-71**: (a) Asymmetric unit; (b) Ligand connection; (c) Coordination configuration of Cu center and (d) SiF_6^{2-} ion connection. Color codes: C, grey; N, blue; F, cyan; Si, Yellow. Brown red polyhedron represents octahedral coordinated Cu atom.

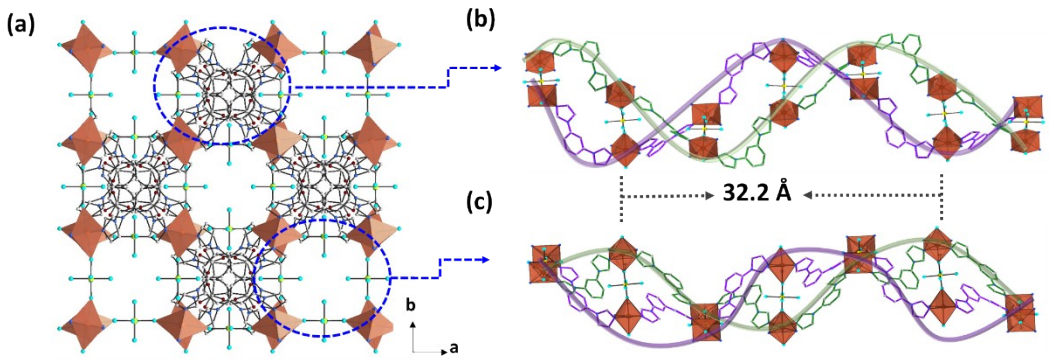

Figure S2. Two helix chains in **NTU-71**.

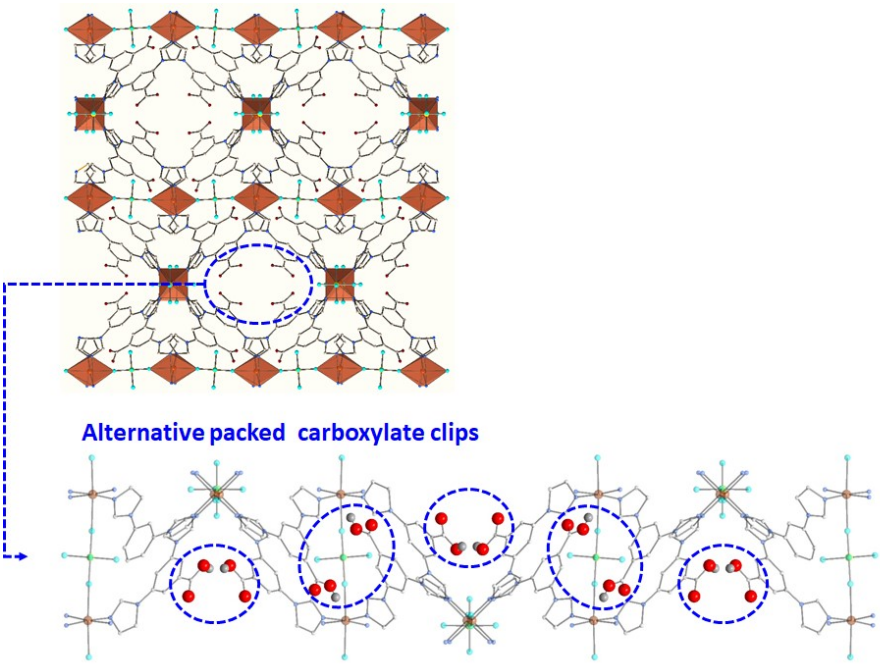

Figure S3. View of the carboxylic pincers that packed alternatively in **NTU-71** along b-axis.

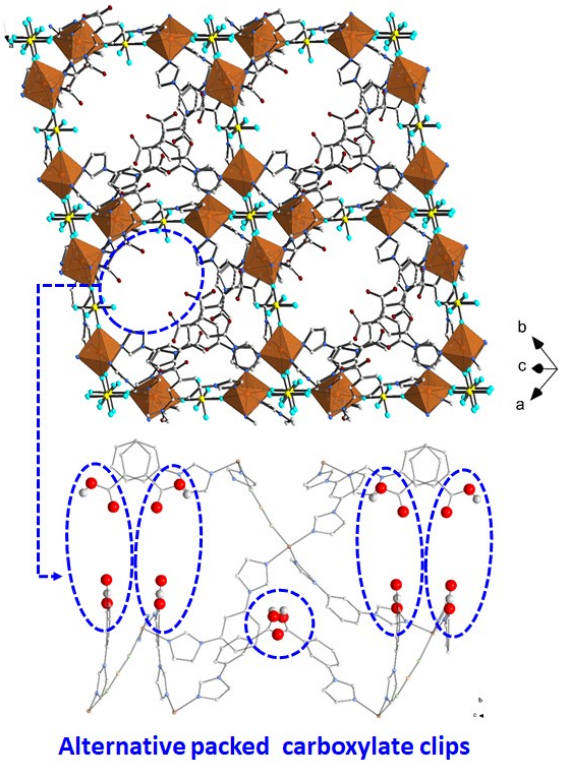

Figure S4. View of the carboxylic pincers that packed alternatively in **NTU-71** along another direction.

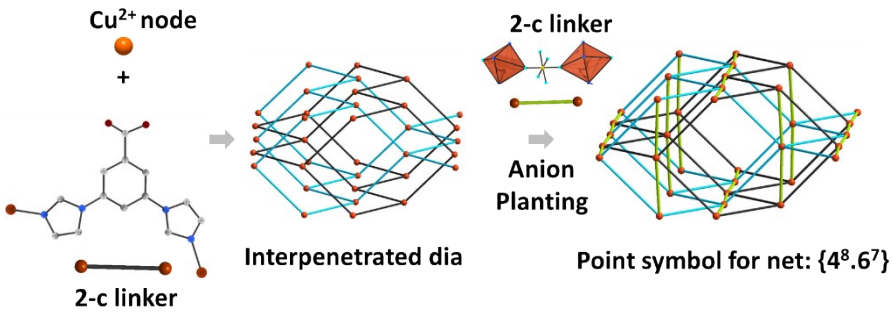

Figure S5. Evolution of **dia** network to a new 6-c topology, exemplified in **NTU-71**.

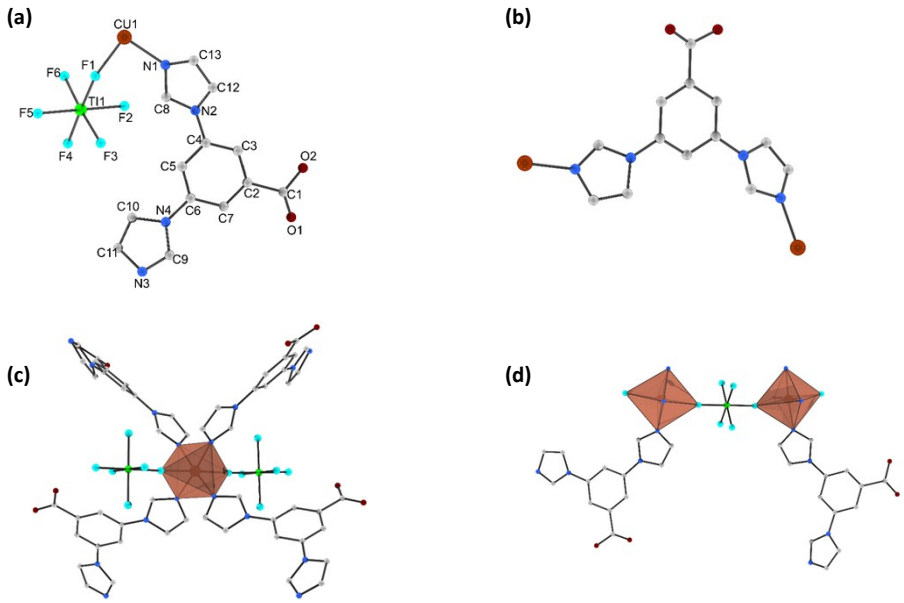

Figure S6. Structure of **NTU-72**: (a) Asymmetric unit; (b) Ligand connection; (c) Coordination configuration of Cu center and (d) SiF_6^{2-} ion connection. Color codes: C, grey; N, blue; F, cyan; Ti, pink. Brown red polyhedron represents octahedral coordinated Cu atom.

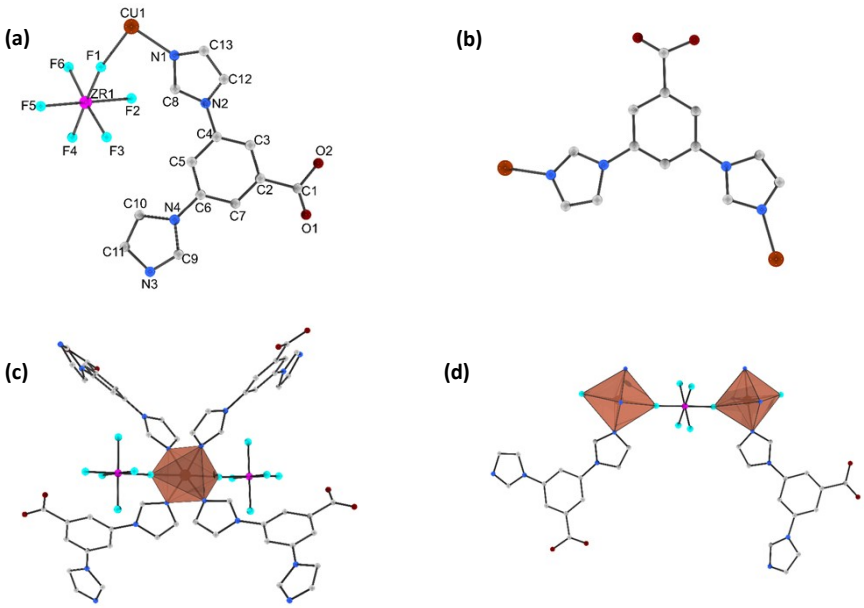

Figure S7. Structure of **NTU-73**: (a) Asymmetric unit; (b) Ligand connection; (c) Coordination configuration of Cu center and (d) ZrF_6^{2-} ion connection. Color codes: C, grey; N, blue; F, cyan; Zr, green. Brown red polyhedron represents octahedral coordinated Cu atom.

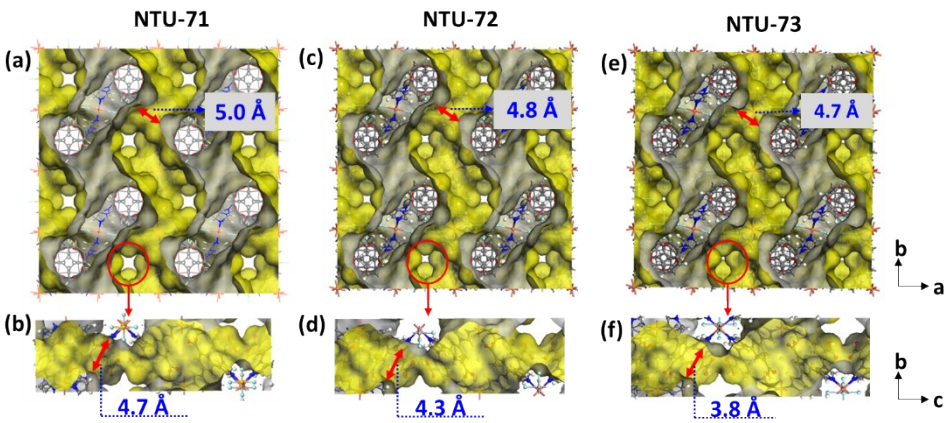

Figure S8. Accessible inner surface (yellow color) and pore size comparison of **NTU-71** (a-b), **NTU-72** (c-d) and **NTU-73** (e-f). Radius of the probe is 1.2 Å

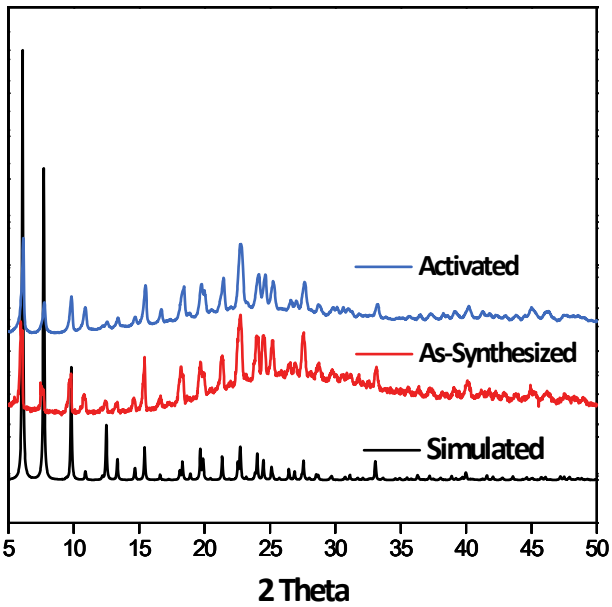

Figure S9. PXRD patterns of **NTU-71**.

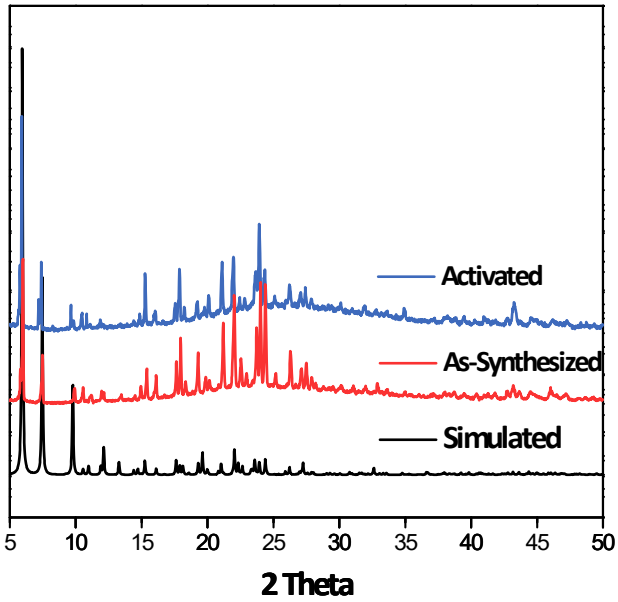

Figure S10. PXRD patterns of **NTU-72**.

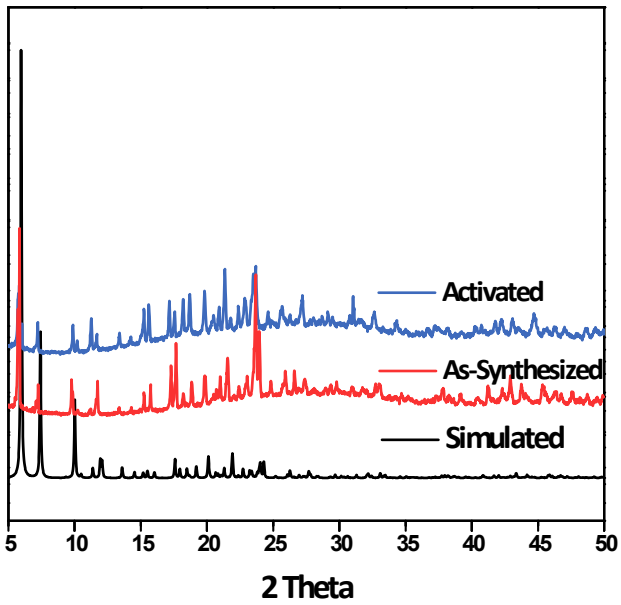

Figure S11. PXRD patterns of **NTU-73.**

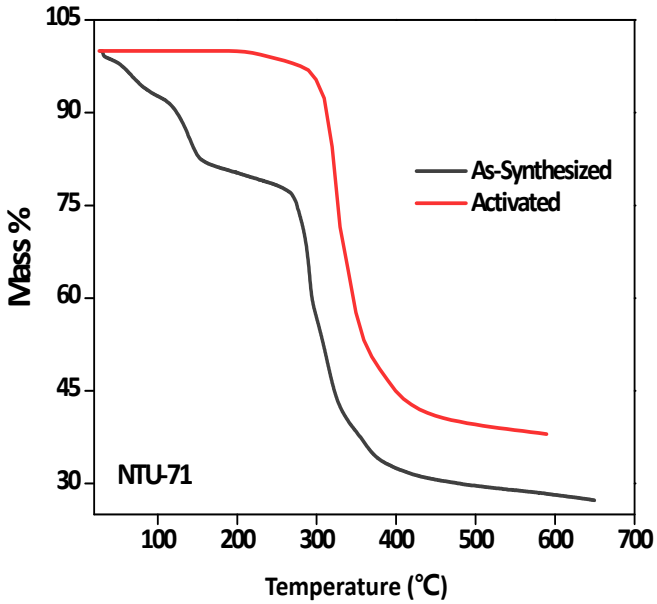

Figure S12. TG curves of as-synthesized and activated **NTU-71.**

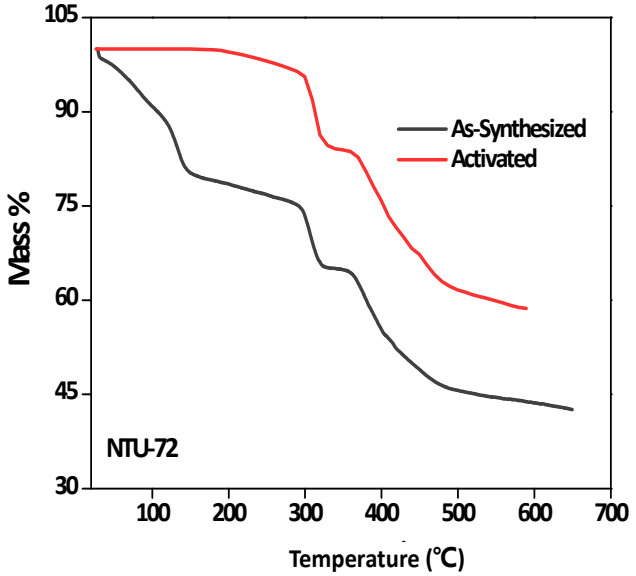

Figure S13. TG curves of as-synthesized and activated **NTU-72.**

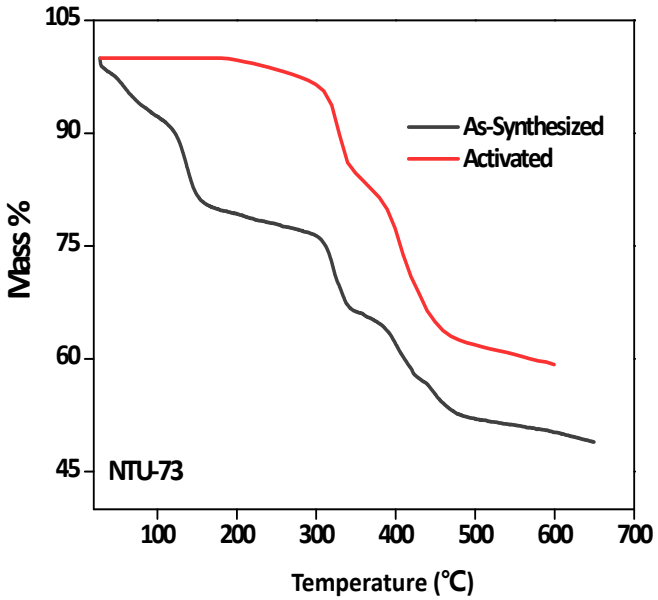

Figure S14. TG curves of as-synthesized and activated **NTU-73.**

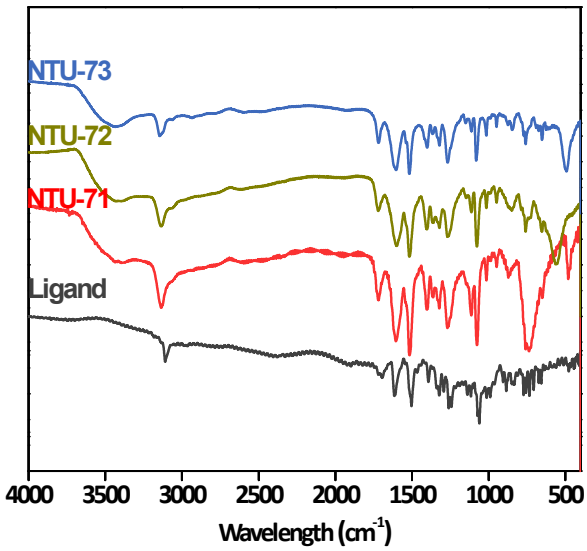

Figure S15. FT-IR spectra for the three PCPs and ligand.

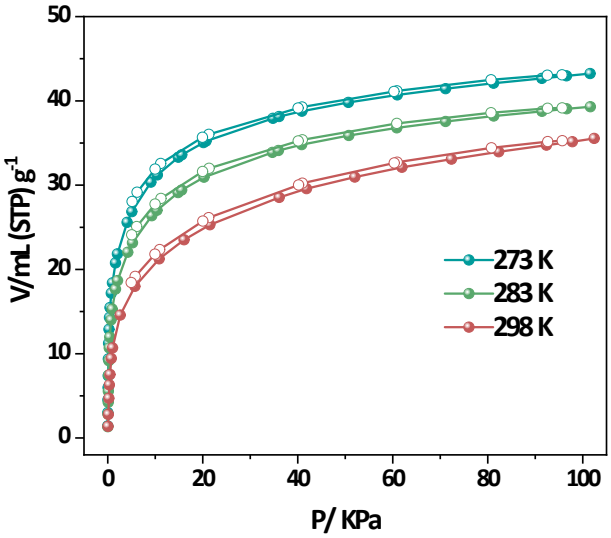

Figure S16. C_2H_2 gas adsorption isotherms of **NTU-71.**

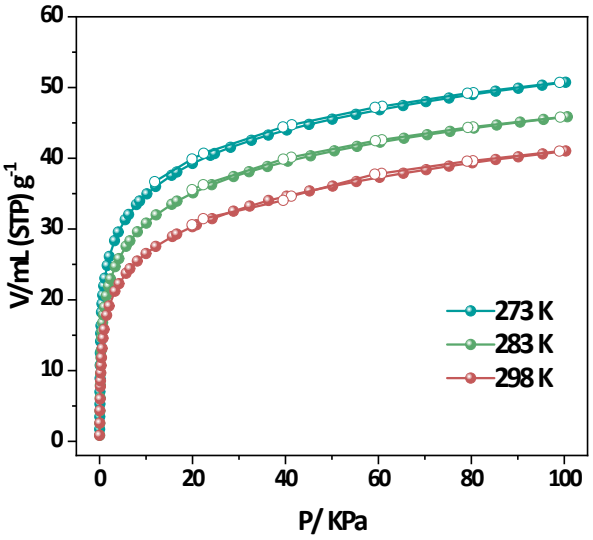

Figure S17. C_2H_2 gas adsorption isotherms of **NTU-72.**

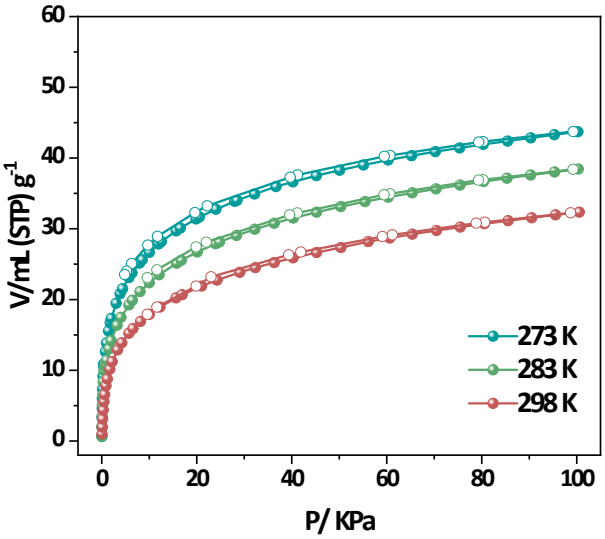

Figure S18. C_2H_2 gas adsorption isotherms of **NTU-73.**

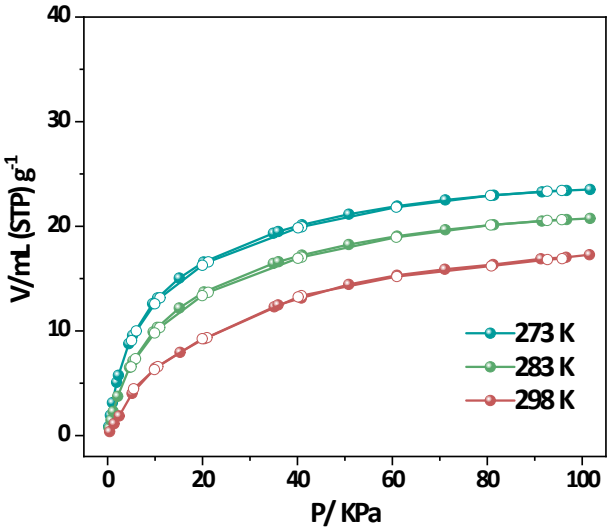

Figure S19. C_2H_4 gas adsorption isotherms of **NTU-71.**

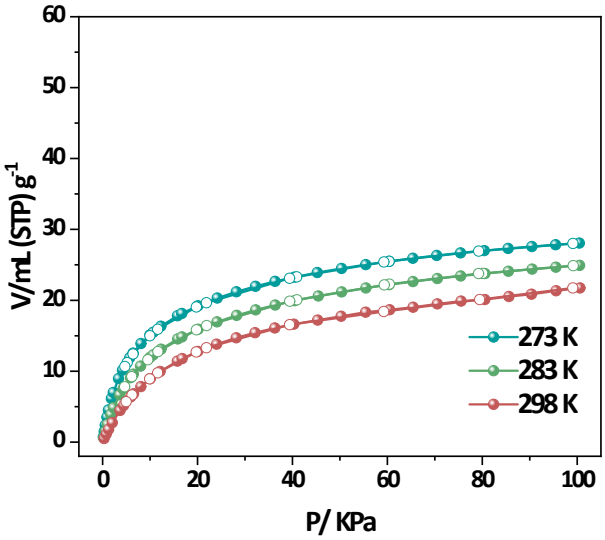

Figure S20. C_2H_4 gas adsorption isotherms of **NTU-72.**

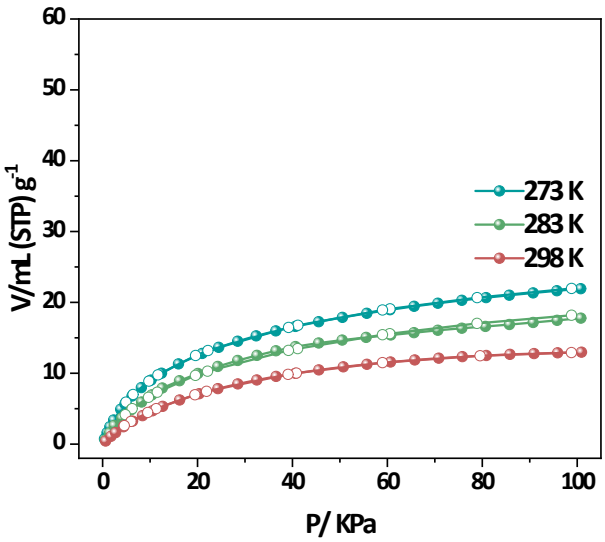

Figure S21. C_2H_4 gas adsorption isotherms of **NTU-73.**

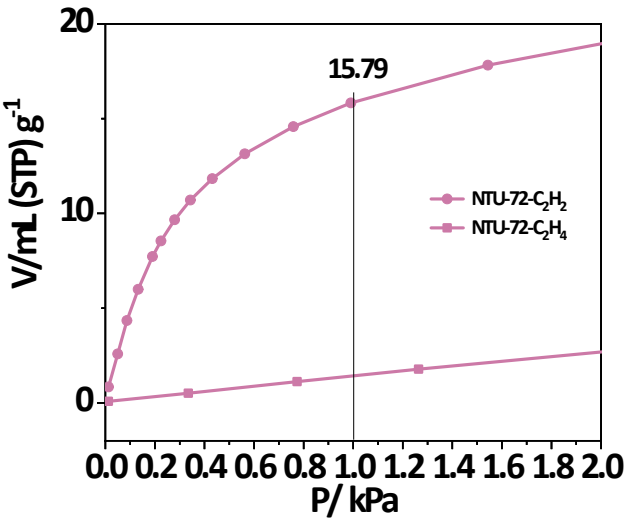

Figure S22. Comparison of the C_2H_2 and C_2H_4 uptakes at 1 kPa, 298 K, in **NTU-72.**

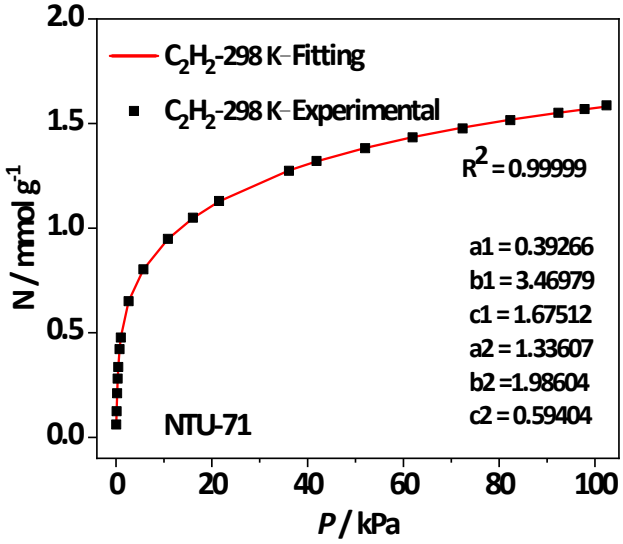

Figure S23. Curves fitting of C_2H_2 gas adsorption isotherms for **NTU-71** at 298 K.

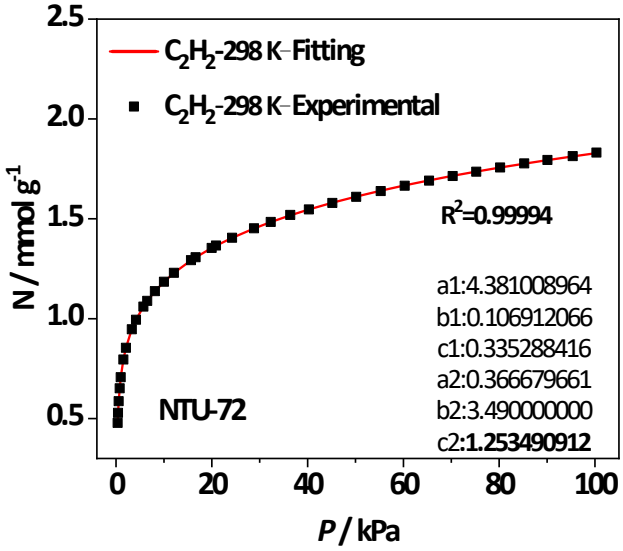

Figure S24. Curves fitting of C_2H_2 gas adsorption isotherms for **NTU-72** at 298 K.

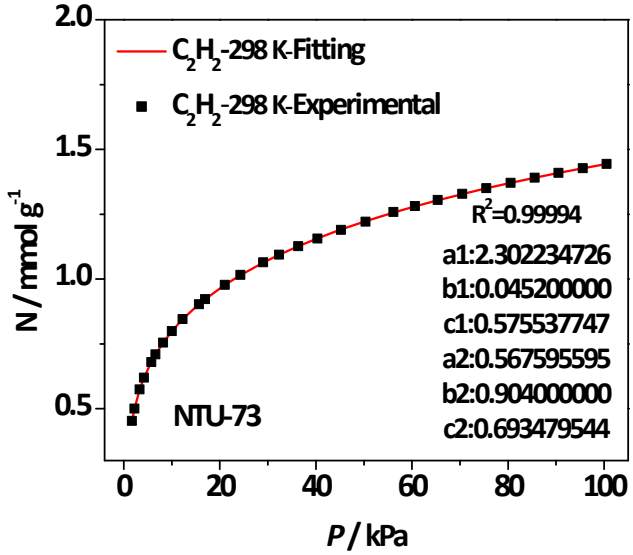

Figure S25. Curves fitting of C_2H_2 gas adsorption isotherms for **NTU-73** at 298 K.

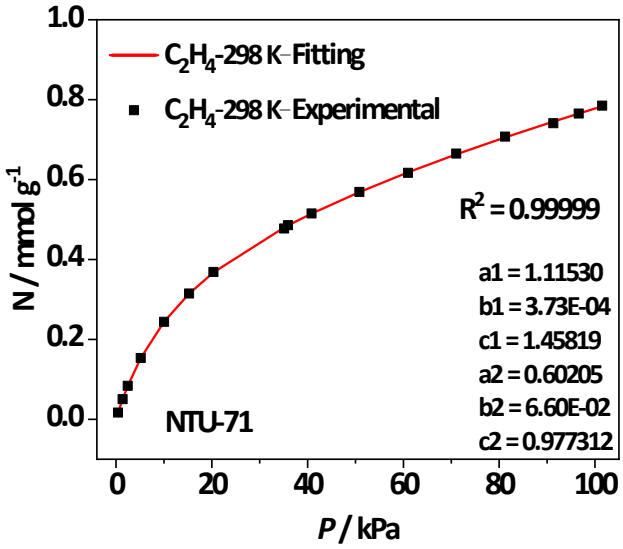

Figure S26. Curves fitting of C_2H_4 gas adsorption isotherms for **NTU-71** at 298 K.

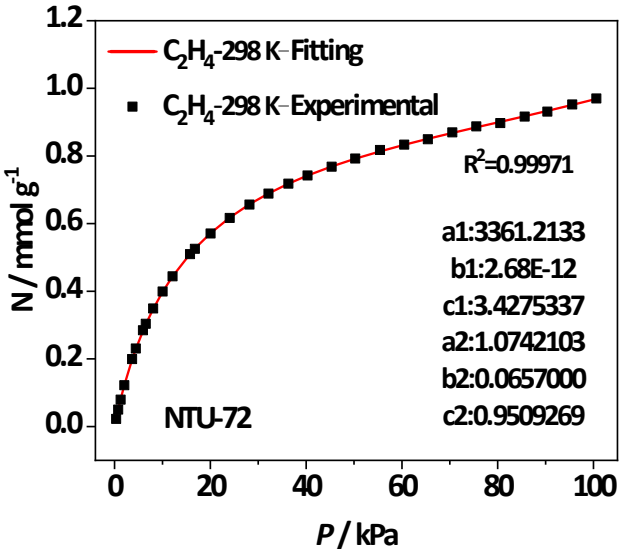

Figure S27. Curves fitting of C_2H_4 gas adsorption isotherms for **NTU-72** at 298 K.

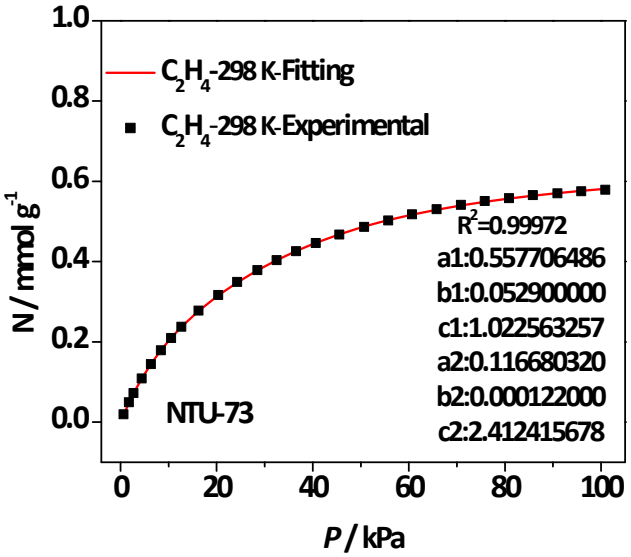

Figure S28. Curves fitting of C_2H_4 gas adsorption isotherms for **NTU-73** at 298 K.

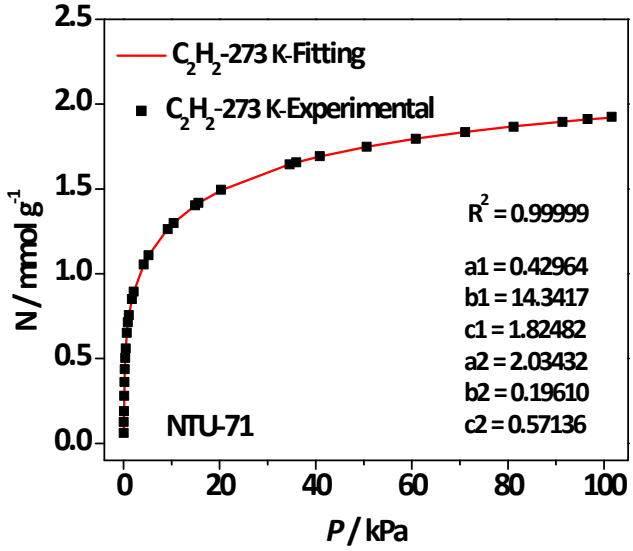

Figure S29. Curves fitting of C_2H_2 gas adsorption isotherms for **NTU-71** at 273 K.

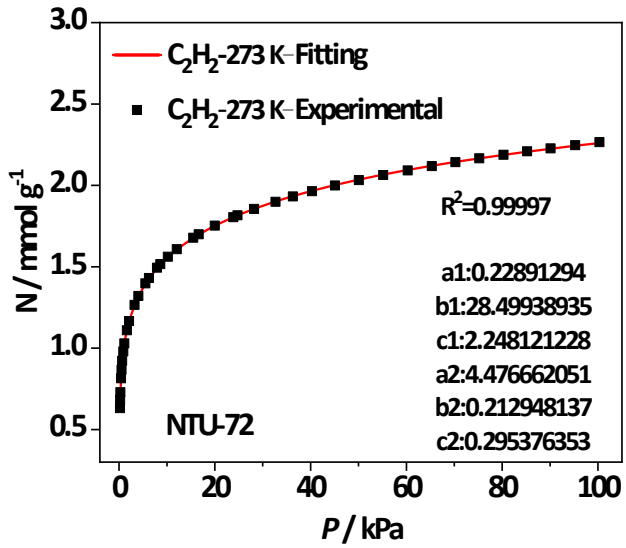

Figure S30. Curves fitting of C_2H_2 gas adsorption isotherms for **NTU-72** at 273 K.

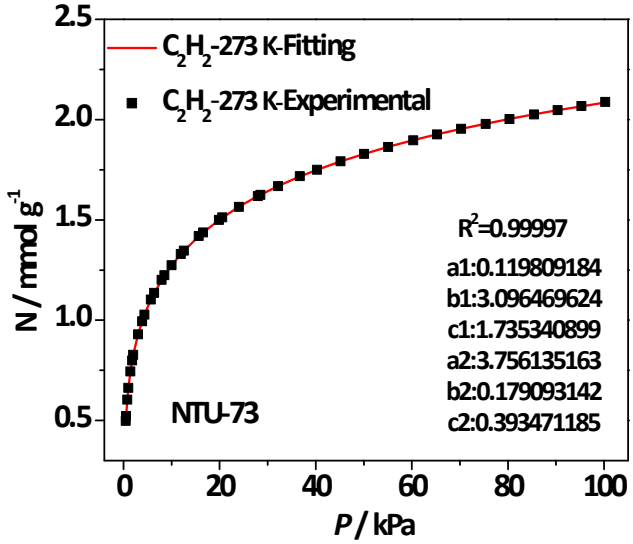

Figure S31. Curves fitting of C_2H_2 gas adsorption isotherms for **NTU-73** at 273 K.

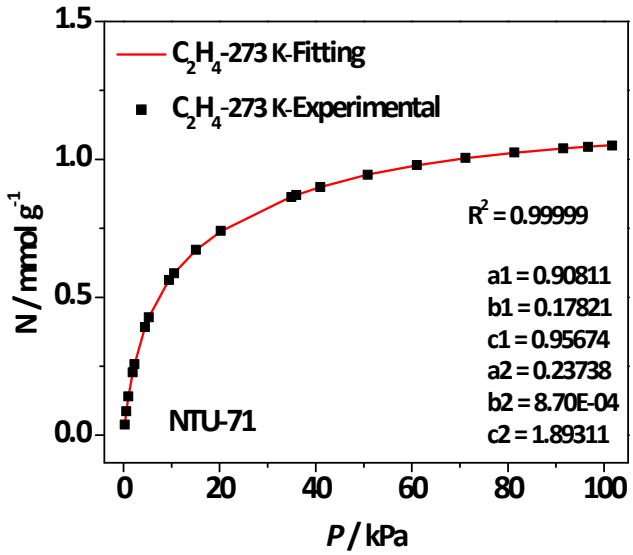

Figure S32. Curves fitting of C_2H_4 gas adsorption isotherms for **NTU-71** at 273 K.

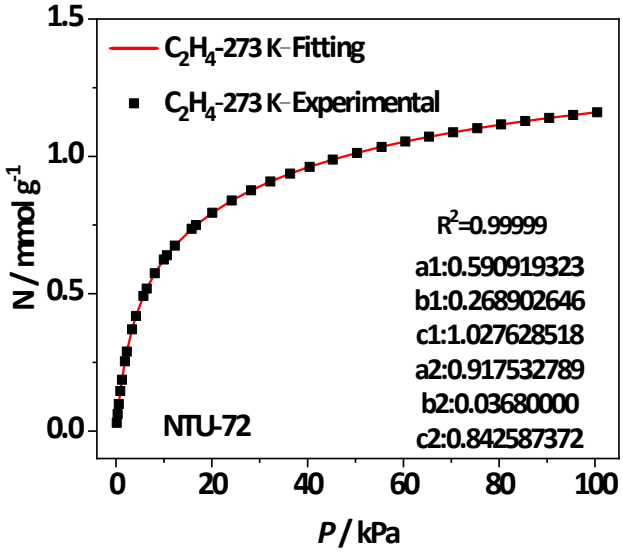

Figure S33. Curves fitting of C_2H_4 gas adsorption isotherms for **NTU-72** at 273 K.

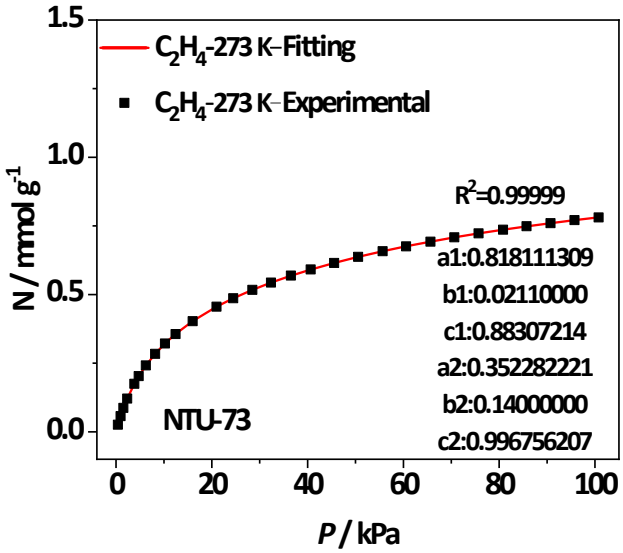

Figure S34. Curves fitting of C_2H_4 gas adsorption isotherms for **NTU-73** at 273 K

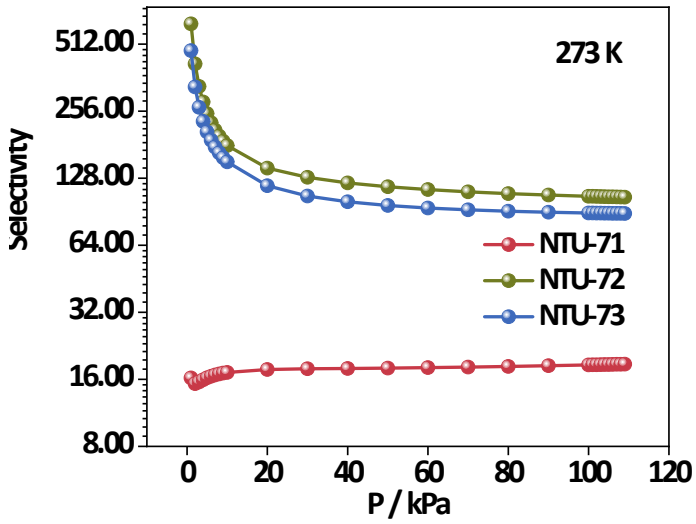

Figure S35. Calculated IAST selectivity for C_2H_2/C_2H_4 mixture (1/99) at 273 K

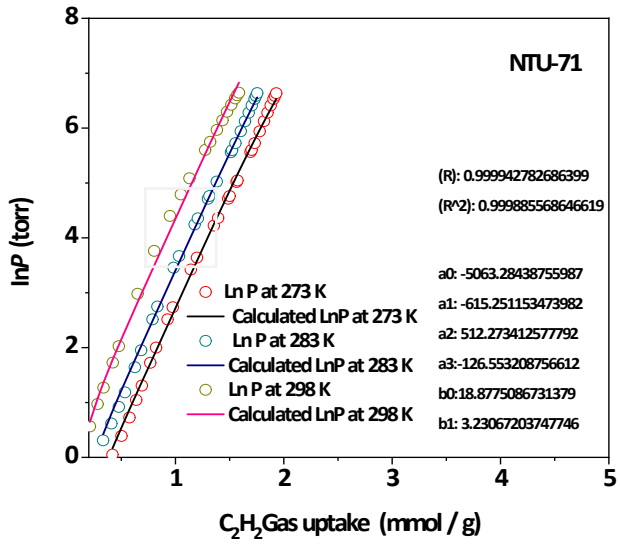

Figure S36. The calculated virial equation isotherms fit to the experimental C_2H_2 data of **NTU-71.**

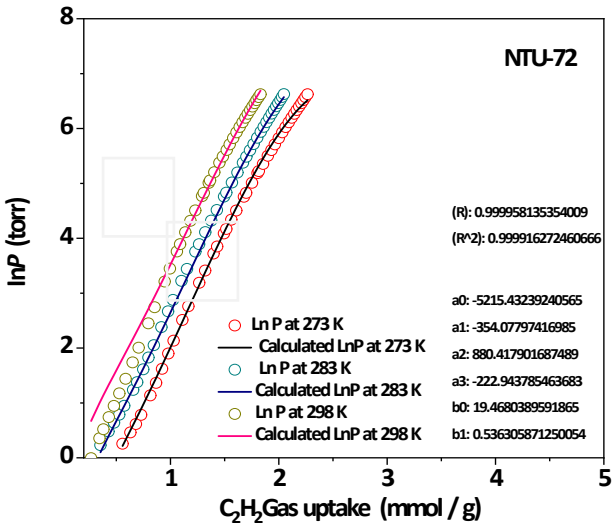

Figure S37. The calculated virial equation isotherms fit to the experimental C_2H_2 data of **NTU-72.**

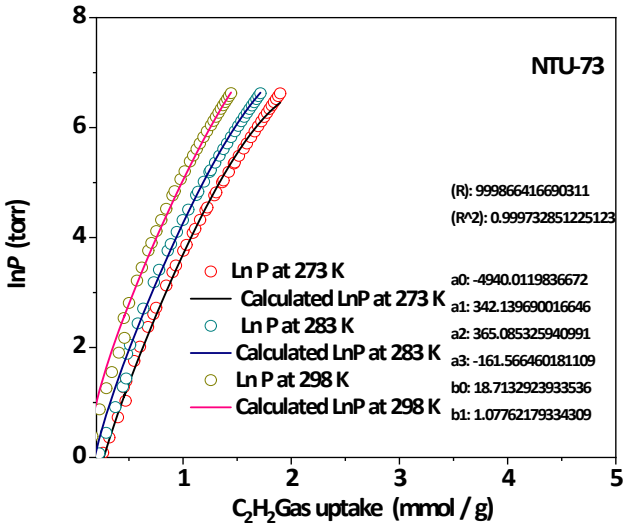

Figure S38. The calculated virial equation isotherms fit to the experimental C_2H_2 data of **NTU-73.**

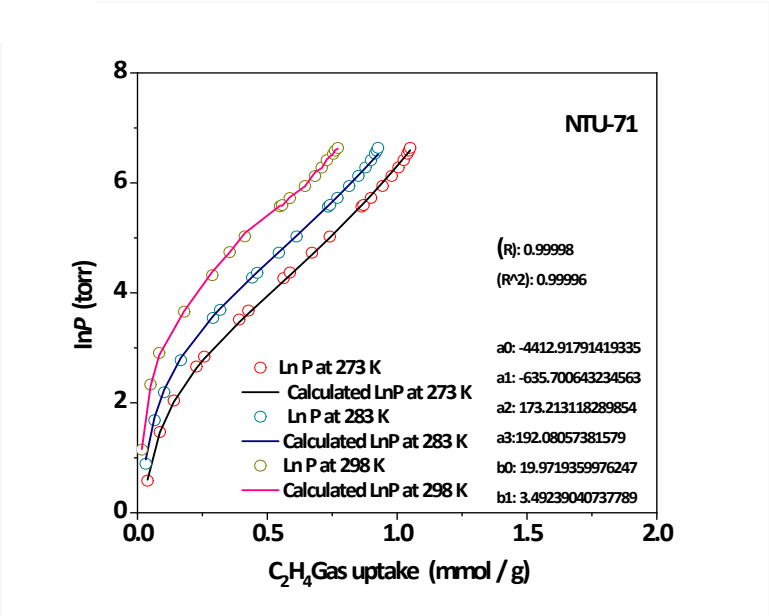

Figure S39. The calculated virial equation isotherms fit to the experimental C_2H_4 data of **NTU-71.**

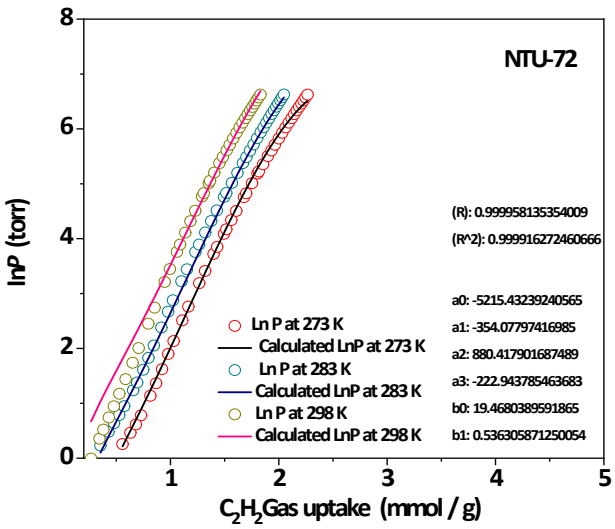

Figure S40. The calculated virial equation isotherms fit to the experimental C_2H_4 data of **NTU-72.**

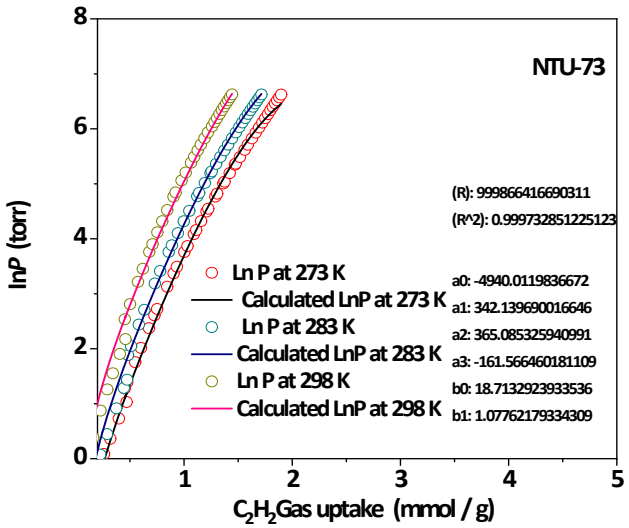

Figure S41. The calculated virial equation isotherms fit to the experimental C_2H_4 data of **NTU-73.**

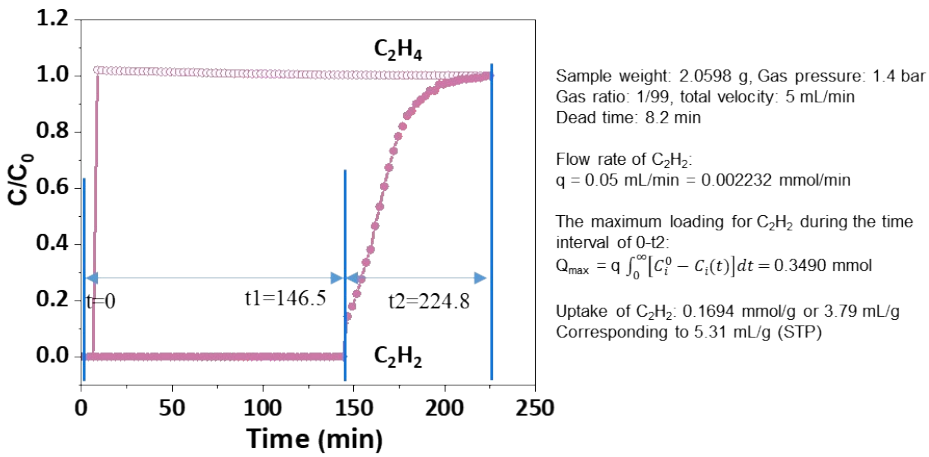

Figure S42. Captured amount of C_2H_2 during breakthrough process in **NTU-72** at 298K.

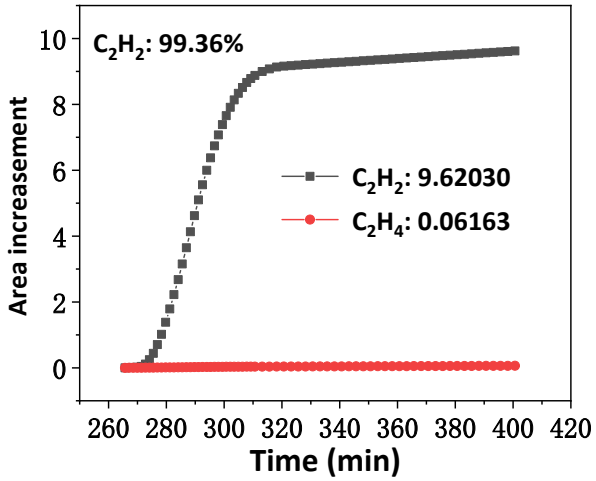

Figure S43. Increased integrity area for C_2H_4 and C_2H_2 during desorption step.

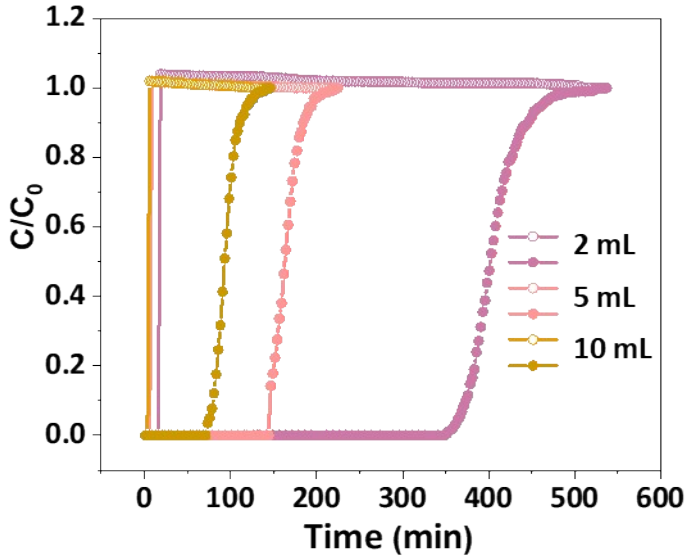

Figure S44. Breakthrough curves of C_2H_2/C_2H_4 on **NTU-72** with different velocities at 298K

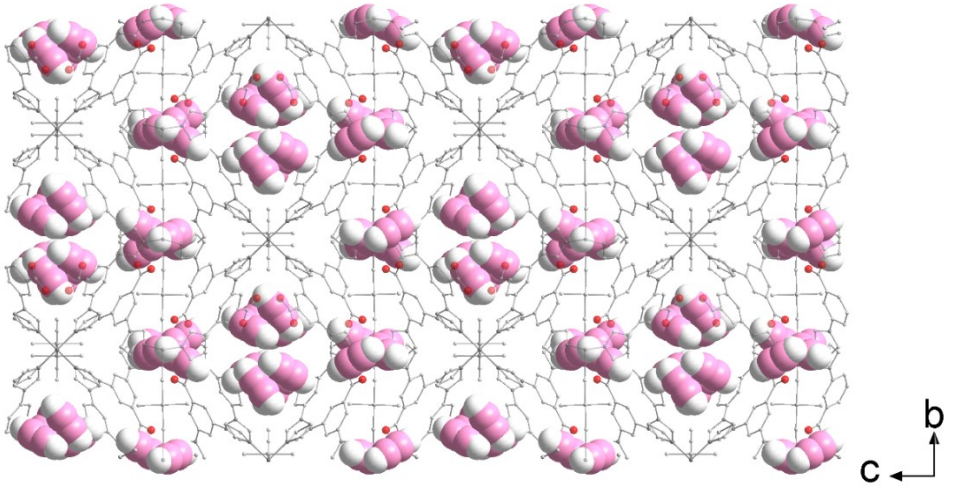

Figure S45. Structure of **NTU-72** ⊃C_2H_2 along a-axis.

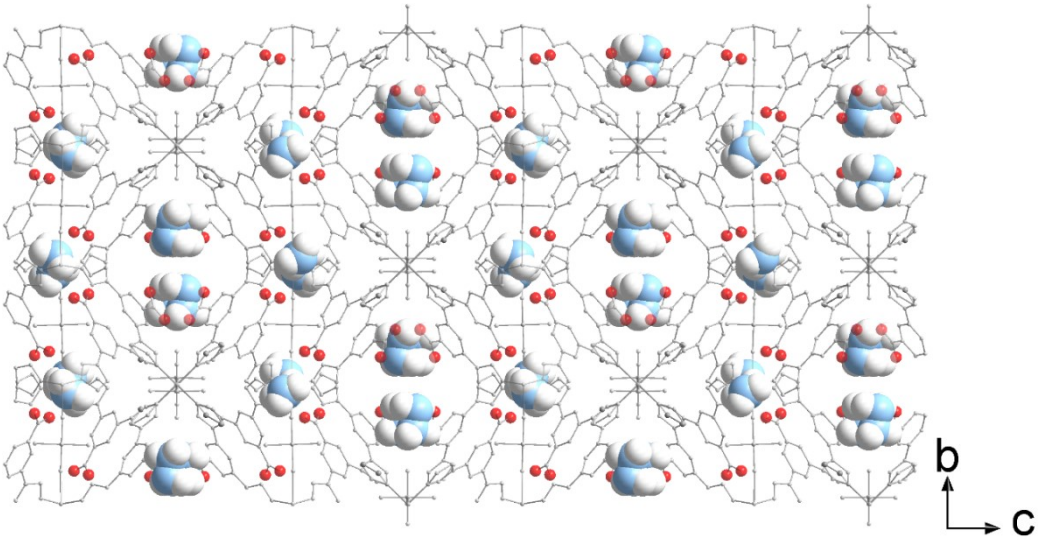

Figure S46. Structure of **NTU-72** ⊃C_2H_4 along a-axis.

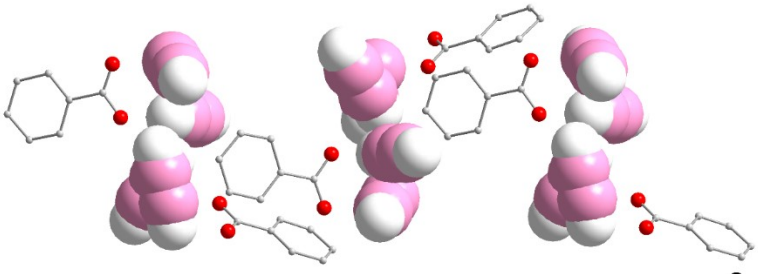

Figure S47. Detailed view of **NTU-72 ⊃C_2H_2**.

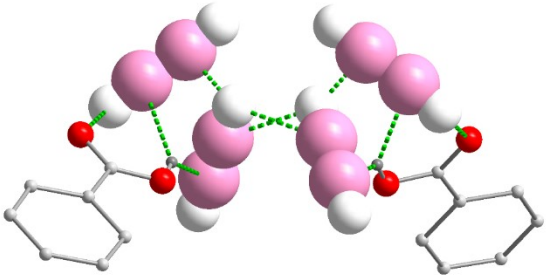

Figure S48. Formed hydrogen bonds between gases and gas-carboxylic pincers in **NTU-72**.

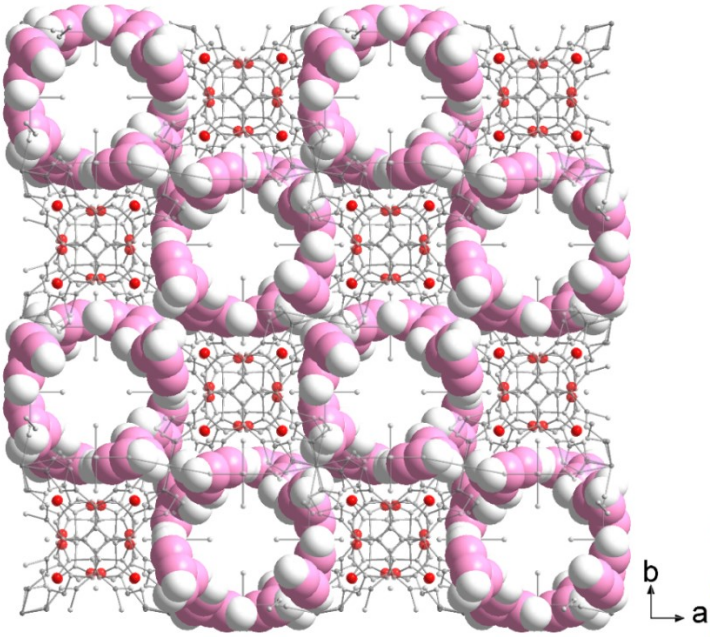

Figure S49. View of the packed C_2H_2 in **NTU-72 ⊃C_2H_2**.

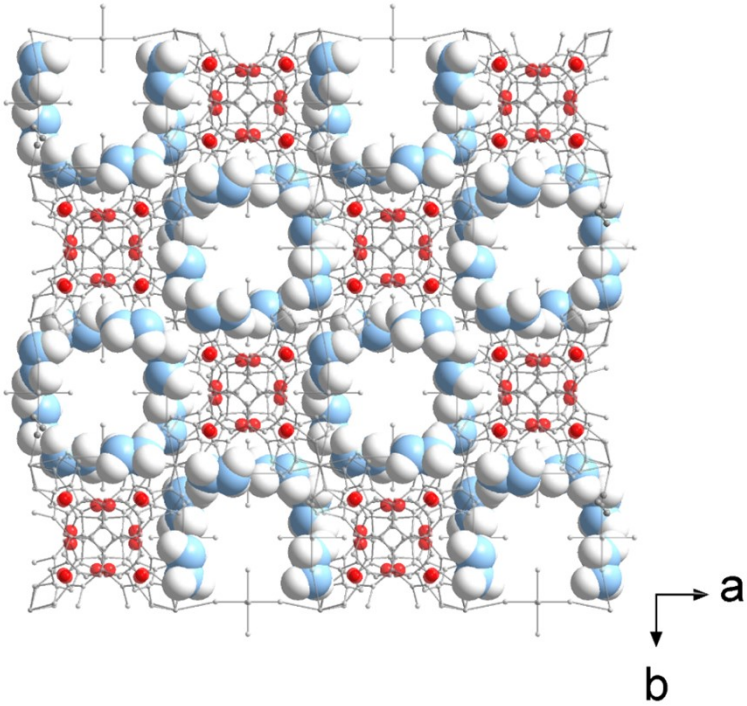

Figure S50. View of the packed C_2H_4 in **NTU-72 ⊃C_2H_4**.

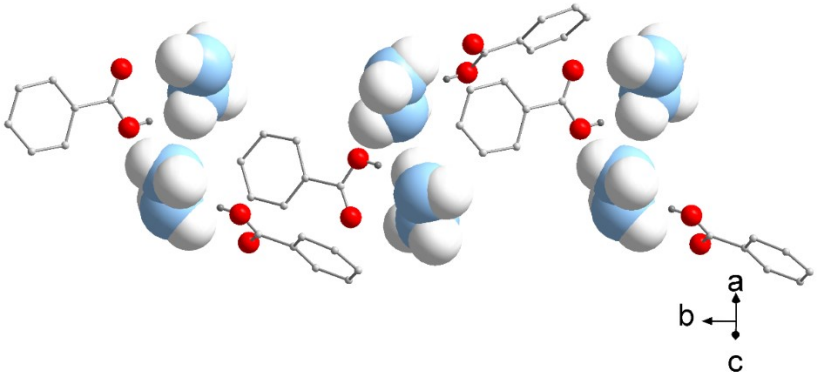

Figure S51. Detailed view of **NTU-72 ⊃C_2H_4**.

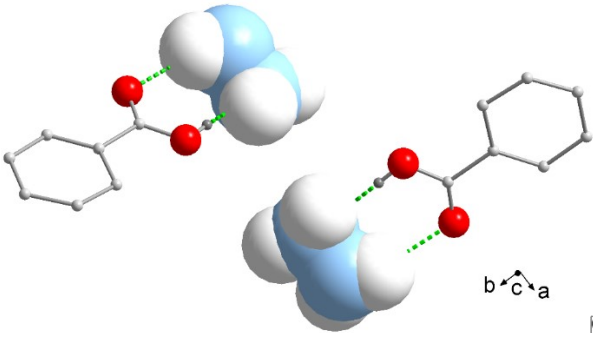

Figure S52. Formed hydrogen bonds between gases and gas-carboxylic pincers in **NTU-72**.

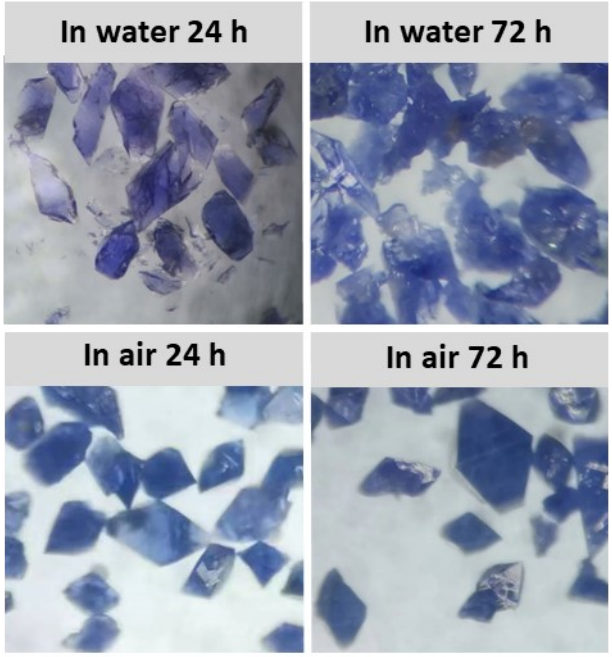

Figure S53. Photograph of **NTU-72** crystals that exposed in air and soaked in water at room temperature.

Table S2. C_2H_2/C_2H_4 selectivity (v/v, 1/99) and uptake ratio of a series of important PCPs.

PCPs	Selectivity, Low pressure	Selectivity, 1 bar	C_2H_2 Uptake (cm^3/g, 1 bar, 298K)	**C_2H_2 purity from desorption**	Velocity of C_2H_2/C_2H_4 ($mL \cdot min^{-1}$)	Refs
NTU-72	441	56.2	41.2	**99.36%**	5	This work
UTSA-300	0.03	$>10^7$	68.9	**99%**	2	5
UTSA-200	3000	6320	81.8	**96.85%**	10	6
ZU-33	4000	1100	79.8	-	1.25	7
ZUL-100	800	175	118.9	-	1.25	8
ZUL-200	60	114	105.1	-	1.25	8
TIFSIX-2-Cu-i	no date	55	91.8	-	10	9
NKMOF-1-Ni	1500	52	61.0	-	10	10
NTU-69	49	45.5	24.6	-	5	11
SIFSIX-2-Cu-i	45	44.5	89.6	-	10	12
Ni-gallate	>100	43.7	80.4	-	1.1	13
NTU-73	147	38.4	32.3	-	-	This work
ZU-62-Ni	>150	37	67.2	-	1.5	14
NTU-71	58	26.2	35.5	-	-	This work
FJU-22	no date	25.8	114.8	-	1.8	15
M'MOF-3	50	24	1.9	-	-	16
Mg-gallate	10	20.9	98.4	-	1.1	13
Co-gallate	20	15.0	87.1	-	1.1	13
APPT-Cd	10	14.6	39.3	-	-	17
TIFSIX-4-Cu-i	9	11	96.3	-	10	9
UTSA-100	5	10.72	95.6	-	2	18
SIFSIX-1-Cu	10.6	7.1	190.4	-	10	12
SIFSIX-3-Zn	6.5	8.82	50.1	-	1.25	19
TJT-100	1.3	1.2	127.7	-	2	20
NUC-2	10	8.1	66.9	-	2	21
JCM-1	9	13.2	75.0	-	-	22

Note:

APPT-Cd: 273 K

M'MOF-3, FJU-22 and UTSA-100: 296 K

UTSA-300 and JCM-1: C_2H_2/C_2H_4 at 1/1 (v/v)

Table S3. Formed hydrogen bonds between **NTU-72** and capture gases.

NTU-72⊃C_2H_2			
D - H…A	D-H(Å)	H…A(Å)	∠D - H…A(°)
C14--H14…O1	0.930	2.309	106.961
O2--H2A…C14	0.850	2.558	145.615
O2--H2A…C15’	0.850	1.871	154.764
C15’--H15’…C15	0.930	1.839	97.963
C15’--H15’…C15’	0.930	2.572	106.417
NTU-72⊃C_2H_4			
C14--H14A…O2	0.857	2.400	152.400
O1--H1A…C15	0.849	2.705	162.578

REFERENCES

1. H. Wang, Y. Duan, Y. Wang, Y. Huang, K. Ge, S. Wang, B. Zheng, Z. Wang, J. Bai and J. Duan, *ACS Appl. Mater. Interfaces*, 2022, **14**, 13550-13559.
2. G. M. Sheldrick, *Acta Crystallogr. Sec. A*, 2008, **64**, 112-122.
3. P. Vandersluis and A. L. Spek, *Acta Crystallogr. Sec. A*, 1990, **46**, 194-201.
4. A. L. Spek, *J. Appl. Crystallogr.*, 2003, **36**, 7-13.
5. R. B. Lin, L. B. Li, H. Wu, H. Arman, B. Li, R. G. Lin, W. Zhou and B. L. Chen, *J. Am. Chem. Soc.*, 2017, **139**, 8022-8028.
6. H. Li, L. Li, R. B. Lin, G. Ramirez, W. Zhou, R. Krishna, Z. Zhang, S. Xiang and B. Chen, *ACS Sustain. Chem. Eng.*, 2019, **7**, 4897-4802.
7. Z. Zhang, X. Cui, L. Yang, J. Cui, Z. Bao, Q. Yang and H. Xing, *Ind. Eng. Chem. Res.*, 2018, **57**, 7266-7274.
8. J. Shen, X. He, T. Ke, R. Krishna, J. M. van Baten, R. Chen, Z. Bao, H. Xing, M. Dinca, Z. Zhang, Q. Yang and Q. Ren, *Nat. Commun.*, 2020, **11**, 6259.
9. A. Bajpai, D. O'Nolan, D. G. Madden, K. J. Chen, T. Pham, A. Kumar, M. Lusi, J. J. Perry, B. Space and M. J. Zaworotko, *Chem. Commun.*, 2017, **53**, 11592-11595.
10. Y. L. Peng, T. Pham, P. Li, T. Wang, Y. Chen, K. J. Chen, K. A. Forrest, B. Space, P. Cheng, M. J. Zaworotko and Z. Zhang, *Angew. Chem. Int. Ed.,* 2018, **57**, 10971-10975.
11. Y. Huang, Y. Xu, B. Zheng, Z. Wang, Q. Dong and J. Duan, *Energ. Fuel.*, 2020, **34**, 11315-11321.
12. X. Cui, K. Chen, H. Xing, Q. Yang, R. Krishna, Z. Bao, H. Wu, W. Zhou, X. Dong, Y. Han, B. Li, Q. Ren, M. J. Zaworotko and B. Chen, *Science*, 2016, **353**, 141-144.
13. J. Wang, L. Li, L. Guo, Y. Zhao, D. Xie, Z. Zhang, Q. Yang, Y. Yang, Z. Bao and Q. Ren, *Chem. Eur. J.*, 2019, **25**, 15516-15524.
14. L. Yang, A. Jin, L. Ge, X. Cui and H. Xing, *Chem. Commun.*, 2019, **55**, 5001-5004.
15. Z. Yao, Z. Zhang, L. Liu, Z. Li, W. Zhou, Y. Zhao, Y. Han, B. Chen, R. Krishna and S. Xiang, *Chem. Eur. J.*, 2016, **22**, 5676-5683.
16. M. C. Das, Q. Guo, Y. He, J. Kim, C. G. Zhao, K. Hong, S. Xiang, Z. Zhang, K. M. Thomas, R. Krishna and B. Chen, *J. Am. Chem. Soc.*, 2012, **134**, 8703-8710.
17. G. Jin, X. Niu, J. Wang, J.-P. Ma, T.-L. Hu and Y.-B. Dong, *Chem. Mater.*, 2018, **30**, 7433-7437.
18. T. L. Hu, H. Wang, B. Li, R. Krishna, H. Wu, W. Zhou, Y. Zhao, Y. Han, X. Wang, W. Zhu, Z. Yao, S. Xiang and B. Chen, *Nat. Commun.*, 2015, **6**, 7328.
19. R.-B. Lin, S. Xiang, W. Zhou and B. Chen, *Chem*, 2020, **6**, 337-363.
20. H. Hao, Y. Zhao, D. Chen, J.-M. Yu, Kui Tan, S. Ma and Z.-M. Z. Yves Chabal, Jian-Min Dou, Zi-Hui Xiao,Gregory Day, Hong-Cai Zhou, and Tong-Bu Lu, *Angew. Chem. Int. Ed.,* 2018, **57**, 16067-16071.
21. H. Chen, G.-L. Zhuang, L. Fan, X. Zhang, L.-N. Gaod and D. Sun, *Chem. Commun.*, 2020, **56**, 2047-2050.
22. J. Lee, C. Y. Chuah, J. Kim, Y. Kim, N. Ko, Y. Seo, K. Kim, T. H. Bae and E. Lee, *Angew. Chem. Int. Ed.,* 2018, **57**, 7869-7873.